

The benefits of elastic full-waveform inversion for subsurface imaging in North Sea shallow-water environments



Andrew Ratcliffe¹, Xiao Chen¹, Zsofia Dobo¹, Pawel Dubiel¹, Jordan Johal¹, James Cooper¹, Nabil Masmoudi², and Tijana Matic¹

<https://doi.org/10.1190/tle44050352.1>

Abstract

Until recently, industrial applications of full-waveform inversion (FWI) have, in practice, been limited by the use of the acoustic wave equation, which considers longitudinal (P) wave velocities but ignores shear (S) wave velocities. This simplifies the differential equations involved by reducing both the parameter space and the computational burden of solving these equations. Moreover, it has resulted in acoustic FWI being adopted as the workhorse tool for velocity model building worldwide, supported by many excellent field data examples. However, in areas of complex geology, strong impedance contrasts can generate highly elastic behavior leading to the breakdown of the acoustic assumption. In these cases, accurate earth models cannot be obtained without considering S-wave velocities via the elastic wave equation. With modern computational power and capacity, elastic FWI is now practical on a large scale, albeit still considerably more computationally demanding than its acoustic counterpart. Many previous studies of elastic FWI typically focused on deepwater areas where large salt structures generate strong elastic effects in the observed seismic data. We offer an alternative perspective on elastic FWI, highlighting its value over acoustic FWI in accurately describing elastic effects observed in shallow-water environments, particularly around the chalk packages prevalent throughout much of the North Sea and adjacent regions.

Introduction

Full-waveform inversion (FWI) has revolutionized subsurface velocity model building. From the pioneering groundwork of the 1980s (Lailly, 1983; Tarantola, 1984), the technology has evolved in the last decade to derive earth models that are not only kinematically accurate but that also reveal subsurface reflectivity with unprecedented resolution (Henin et al., 2023; Wei et al., 2023; Dinh et al., 2024). FWI is a highly complex and nonlinear optimization problem where the unknowns are earth model parameters (typically compressional velocity, although we may also consider shear velocity, density, anisotropy, and other parameters as unknowns) distributed over a discretized grid of subsurface locations. There may be millions or even billions of these unknowns in an industrial application of FWI; hence, there are considerable computational demands associated with its deployment on a commercial scale.

Several factors influence the computational cost of FWI, including the complexity of the wave equation used for the propagation as well as how coarsely the internal engine used to solve

this equation can be discretized (in time and space). Early industry FWI successes (Plessix, 2009; Sirgue et al., 2009) were restricted to low frequencies (to allow aggressive discretization without adversely affecting the results) and simple wave equations. Modern implementations take advantage of improvements in computer hardware to push FWI to higher frequencies, yielding significant benefits in terms of earth model resolution. The advent of FWI imaging (Kalinicheva et al., 2020; Zhang et al., 2020) has shown that, at high frequencies, FWI can be used to obtain subsurface images superior to those derived from conventional primary-only imaging methods. Nonetheless, until recently, these applications largely persisted with the simplified acoustic wave equation.

Wavefield propagation in the earth is governed by the elastic (or viscoelastic) wave equation, which offers a complete description of the waves observed in a seismic experiment. It considers both longitudinal, compressional (P) waves and transverse, shear (S) waves. In some geologic contexts, contributions from shear waves in the observed data are small, and the acoustic approximation is sufficiently accurate to explain the observed data. Solutions of the acoustic wave equation are easier to obtain, so it is an attractive option for FWI. In recent years, however, the reduced physics in the acoustic wave equation has come under increasing scrutiny. Complex geologies often feature highly reflective interfaces, giving rise to abundant mode conversions between P and S waves, which are described accurately only with the elastic wave equation. Previous strategies to address this issue have typically been based on the acoustic approximation, while employing some method to mitigate the elastic effects (Hobro et al., 2014; Agudo et al., 2018; Sun and Alkhalifah, 2021). However, approaches of this kind can offer only limited benefits, and it is inevitable that FWI must consider the full, elastic wave equation if it is to succeed in environments where strong elastic effects are found in the observed data.

Elastic FWI

The recent emergence of elastic FWI (see, for example, Plessix and Krupovnickas, 2021; Wang et al., 2021) has generated significant interest. Due to its efficiency, acoustic FWI may still be preferred by many, but this landscape is changing quickly with the value of elastic FWI becoming firmly established. Several previous studies demonstrating the advantages of elastic FWI have concentrated on deepwater areas dominated by complex salt bodies (Plessix and Krupovnickas, 2021; Wu et al., 2022; Pérez Solano and Plessix, 2023; Richardson et al., 2023; Zhang et al., 2023). In this article, we focus on an environment that has received

Manuscript received 8 January 2025; accepted 10 February 2025.

¹Viridien, Crawley, UK. E-mail: andrew.ratcliffe@viridiengroup.com; xiao.chen@viridiengroup.com; zsofia.dobo@viridiengroup.com; pawel.dubiel@viridiengroup.com; jordan.johal@viridiengroup.com; james.cooper@viridiengroup.com; tijana.matic@viridiengroup.com.

²Formerly Viridien; presently bp, Sunbury, UK. E-mail: nabil.masmoudi@bp.com.

Redistribution subject to SEG license or copyright; see Terms of Use at <http://library.seg.org/page/policies/terms>. DOI: 10.1190/tle44050352.1

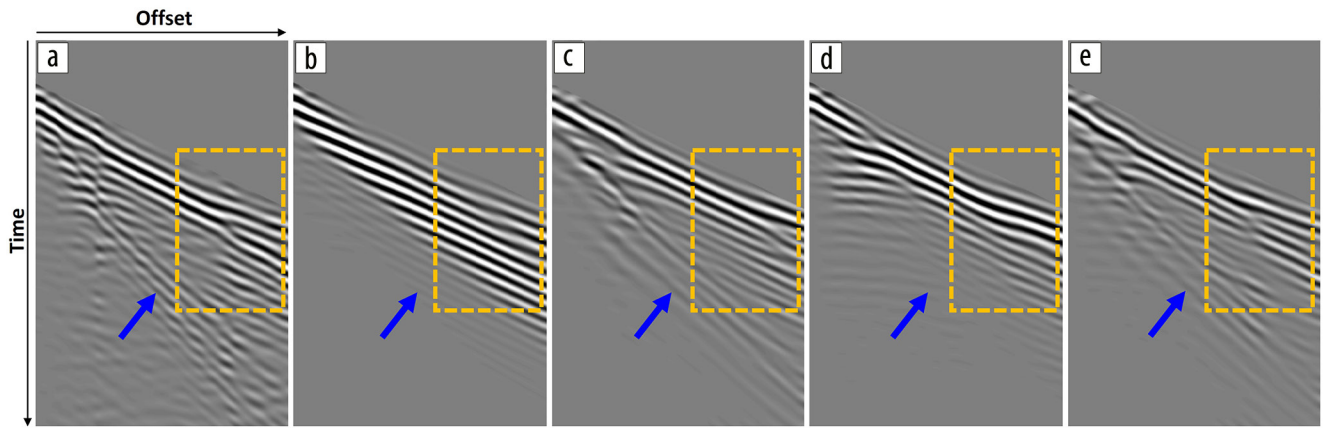


Figure 1. Observed and modeled data at 5 Hz in an area where chalk outcrops at the seabed: (a) observed data; (b) acoustically modeled data and (c) elastically modeled data using a legacy velocity model; (d) acoustically modeled data after a 6.5 Hz acoustic FWI; and (e) elastically modeled data after a 6.5 Hz elastic FWI. Modified from Johal et al. (2024).

much less attention in the literature: the chalk package, with its variable thickness and rugosity, that is present throughout much of the North Sea. We consider the depth of the chalk and the impact this has on FWI as it varies from shallow to deep. We use the elastic FWI methodology discussed in Masmoudi et al. (2022, 2023). We also discuss the influence that the shallow-water nature of the area has on FWI and the challenges this brings. Throughout, we show both elastic and acoustic results, in both cases inverting only for the P-wave velocity to ensure a fair comparison between the two approaches. We include field data examples from towed-streamer and ocean-bottom node (OBN) acquisitions to highlight improved exploration and development opportunities in this mature hydrocarbon province. Finally, we discuss some common trends and features of these examples to offer improved understanding of how and why elastic FWI has been of benefit.

Very shallow chalk

The Breagh gas field is a Carboniferous sandstone structure in the southern North Sea. The shallow overburden in this region is characterized by high-velocity Cretaceous chalk, which varies in depth from 1 km up to the seafloor. Immediately beneath this, low-velocity Jurassic sediments form a highly elastic interface with the chalk, generating velocity contrasts up to 2000 m/s. In addition, the shallow (50–80 m) water bottom itself represents a large impedance contrast due to the rapid change in density between water and sediment. This gives rise to a potentially complex interplay between two neighboring and highly elastic boundaries.

Johal et al. (2024) compared elastic and acoustic FWI in this region for two legacy narrow-azimuth, towed-streamer acquisitions. Figure 1 shows common shot gather modeling in the region where the chalk layer outcrops at the seabed. For 5 Hz modeled data using the legacy model, there is a clear improvement moving from acoustic (Figure 1b) to elastic modeling (Figure 1c), with the latter better describing the far-offset train of first-arrival events (yellow boxes) recorded in the observed data (Figure 1a), as well as capturing the surface (Scholte) waves (blue arrows) seen in the observed data but missing from the acoustically modeled data. Data modeled after a subsequent application of 6.5 Hz acoustic (Figure 1d) or elastic (Figure 1e) FWI (run in a like-for-like

manner) demonstrate that both inversions reduce the misfit with the observed data, but the elastic FWI still offers a more accurate representation of the far-offset arrival train. It is likely that the reduced misfit obtained with acoustic FWI has, in part, been manufactured by erroneous updates in the inversion, such updates needing complex workflows to mitigate the limitations that elastic FWI resolves naturally (see, for example, Refaat et al., 2021; Masmoudi et al., 2022, 2023).

Following this initial analysis, acoustic and elastic FWI were compared at 10 Hz down to 1.5 km in depth. This is beyond the maximum depth of both the chalk package and the diving-wave penetration, which is limited to approximately 1 km by the acquisition. The resulting P-wave velocities (V_p), overlain on a seismic image, are shown in Figure 2. Both acoustic (Figure 2a) and elastic (Figure 2b) FWI exhibit a slowdown at the boundary of the base chalk (white dashed line). However, we see a much stronger contrast and clearer delineation of this boundary with the V_p model obtained from elastic FWI. This is verified by the velocity profiles in Figure 2c (at the locations of the blue dashed lines on Figures 2a and 2b), where the elastic FWI (green) captures the increasing velocity gradient through the chalk and maintains the true magnitude of the base chalk velocity contrast (black box), giving a very close match to the sonic log (blue). In contrast, the acoustic FWI (orange) deviates significantly from the sonic through the chalk layer and the Jurassic sediments beneath. This is an example of acoustic FWI manufacturing erroneous updates to reduce misfit in the presence of elastic effects.

A subsequent 15 Hz elastic update down to the target level of approximately 3 km shows further uplift, particularly around the deeper salt structures present in the region. This update is driven by reflection energy only as the recorded diving waves do not penetrate to this depth. Figure 3e compares velocity profiles for a sonic log (blue), the legacy model (white), and the 15 Hz elastic FWI update (green). The fast basal anhydrite layer (black arrows) seen on the sonic is absent from the legacy model but is well described by elastic FWI. Figures 3a and 3b show the legacy and final elastic FWI models, respectively, overlain on corresponding 40 Hz reverse time migrated (RTM) images. The speedup in the anhydrite layer is again evident after elastic FWI. The same

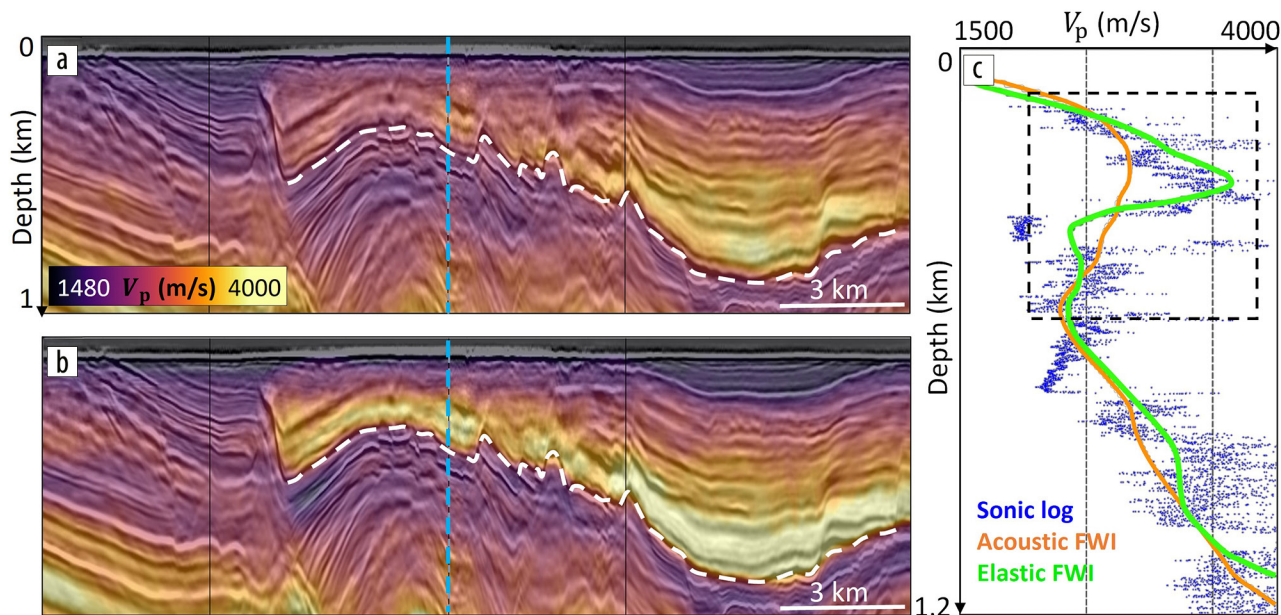


Figure 2. A comparison of 10 Hz acoustic FWI and elastic FWI around the shallow chalk: V_p from (a) acoustic and (b) elastic FWI, both overlain on a seismic image; (c) velocity profiles for acoustic (orange) and elastic (green) FWI compared to a sonic log (blue). The base chalk boundary and the well location are indicated, respectively, by the white and blue dashed lines on (a) and (b).

RTM images are shown separately in more detail in Figures 3c and 3d, where the structural improvements from elastic FWI around the salt are clear, allowing a more accurate geologic interpretation of the reservoir region.

Shallow chalk

The previous example illustrates the difficulties faced by acoustic FWI in the presence of an unusually shallow chalk layer. Elsewhere in the North Sea, relatively shallow chalk is still widespread. Dobo et al. (2024a) showed acoustic and elastic FWI results for a shallow-water OBN survey over the Buzzard field in the UK North Sea, where the chalk layer can be found at depths of up to 1 km. Below the deeper Base Cretaceous Unconformity (BCU), hydrocarbon-bearing sands are a key target in this area. The chalk exhibits velocities up to 4000 m/s while abutting slower clastic rocks with velocities of approximately 2000 m/s, again giving rise to a highly elastic interface. The chalk structure at Buzzard is broadly tabular, but at the nearby Golden Eagle field, it is highly rugose. Dobo et al. (2024b) compared acoustic and elastic FWI results for an OBN survey at Golden Eagle. We show results from both areas here.

Figure 4 illustrates results of acoustic and elastic FWI for Buzzard (Figures 4a–4d) and Golden Eagle (Figures 4e–4h) run in a like-for-like manner. The key top chalk, base chalk, and BCU markers are annotated on each panel in cyan. Figures 4a (Buzzard) and 4e (Golden Eagle) show 15 Hz acoustic FWI results. In both cases, the acoustic FWI velocity profiles, in Figures 4d and 4h respectively, highlight significant deviations in the model update (yellow) from the sonic logs (blue) at the top/base chalk boundaries, creating a visible “halo” effect on the associated V_p model displays (Figures 4a and 4e). Similarly, the inverted velocities around the deeper BCU target diverge from the sonics, which is a consequence of the erroneous update in the chalk overburden. Figures 4b and 4f show analogous results but for a 15 Hz elastic FWI. The halo

effect has been avoided, with the chalk boundaries better resolved and better aligned to the well markers. The velocity profiles show a good match between the elastic FWI (green) and the sonic logs at both the chalk and the target BCU levels. Figures 4c and 4g show the effects of increasing the maximum frequency of the elastic FWI update to 30 Hz (Buzzard) and 25 Hz (Golden Eagle). The match between elastic FWI (white) and the sonic logs is further improved, and fine layering is apparent alongside other structural details, such as the small-scale rugosity of the top chalk at Golden Eagle (white arrow).

In Figure 5, we further verify the benefits of elastic FWI on Golden Eagle by comparing conventional migration using a legacy model (Figure 5a) (obtained from tomography and well calibration) and the 25 Hz elastic FWI model (Figure 5b). The rugosity of the chalk in this region makes it difficult to fully appreciate the differences between these two results, but the orange arrows highlight some of the areas where the elastic FWI simplifies the depth structure relative to the legacy model, which is especially important for improving the reservoir characterization of the field.

High-wavenumber structural information in the V_p models can be revealed more clearly by forming the FWI image (Zhang et al., 2020), giving a direct measure of reflectivity that can be compared against the results of conventional seismic imaging. In Figure 6a, we show the elastic FWI image derived from the 30 Hz model update at Buzzard, with the corresponding 30 Hz RTM result shown in Figure 6b. The locations of four wells are annotated by the markers on these figures, with corresponding logs shown in Figures 6c–6f. Structurally, there is good qualitative agreement between the results. The base chalk package is known to be divided across two formations: the Plenus Marl (green markers) and the slightly deeper Rødby (orange arrows). The elastic FWI image correctly captures the amplitude relationship between the two formations, with the corresponding V_p model (Figures 6c–6f, white curves) giving excellent agreement with the sonics (blue

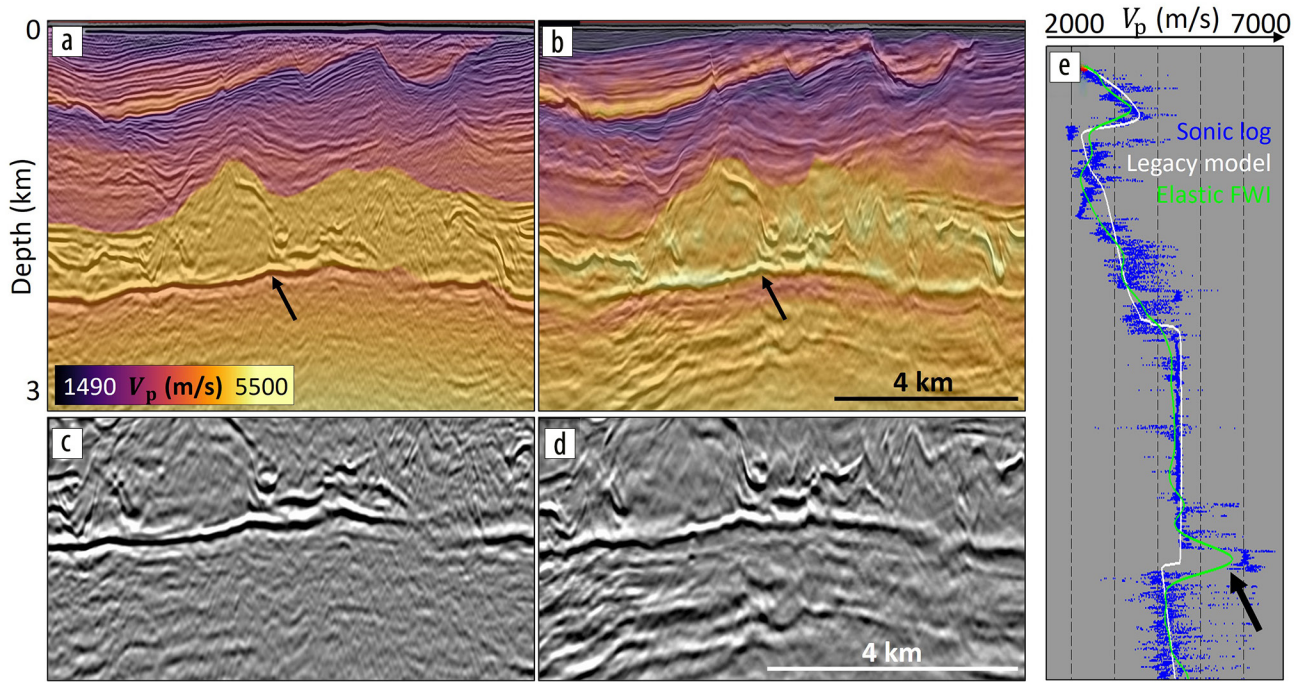


Figure 3. Elastic FWI update down to the target level: (a) legacy V_p model and (b) 15 Hz elastic V_p model, both overlain on their corresponding 40 Hz RTM images; (c) and (d) details of the same RTM images shown in (a) and (b), respectively; (e) velocity profiles for legacy (white) and 15 Hz elastic (green) models, compared to a sonic log (blue).

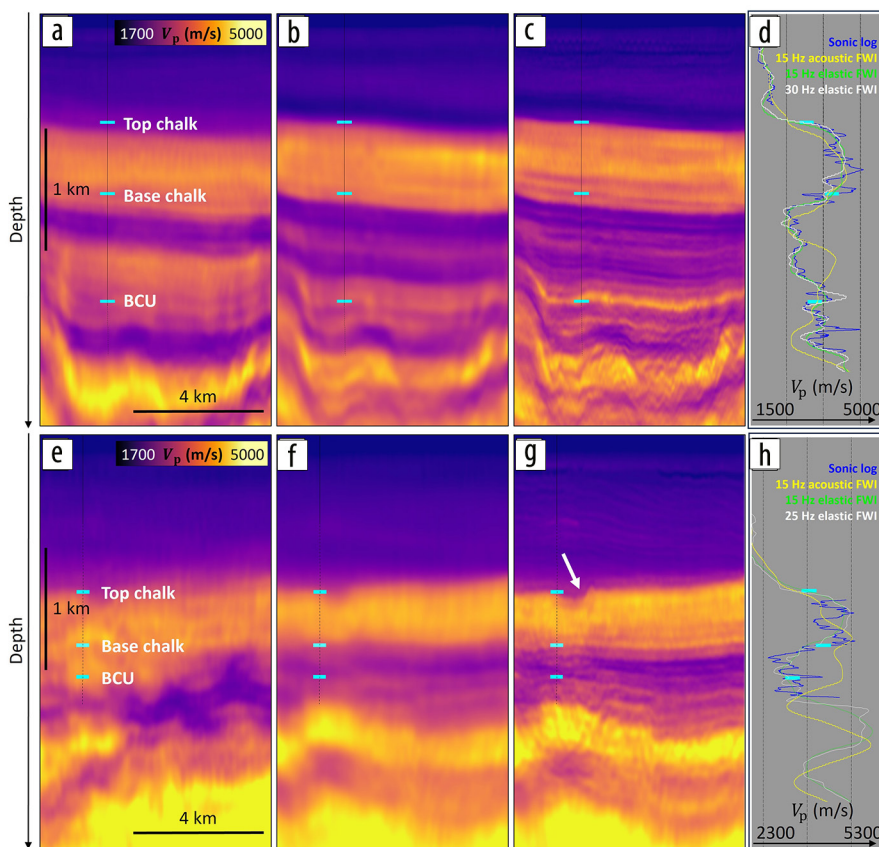


Figure 4. Acoustic versus elastic FWI for (a–d) Buzzard and (e–h) Golden Eagle: (a) and (e) 15 Hz acoustic FWI; (b) and (f) 15 Hz elastic FWI; (c) 30 Hz elastic FWI for Buzzard; (g) 25 Hz elastic FWI for Golden Eagle; (d) and (h) velocity profiles for acoustic FWI (yellow), elastic FWI (green/white), compared against the sonic log (blue). Key horizons are indicated by the cyan markers. Modified from Dobo et al. (2024a, 2024b).

curves) throughout the base chalk and at the BCU target.

Deeper chalk

In other regions of the North Sea, the chalk layer descends beyond 2.5 m in depth. In these settings, complex geology above the chalk can bring additional challenges to FWI. Previously, Chen et al. (2024) reported elastic FWI results for an OBN survey in the Norwegian North Sea in an area characterized by several distinctive geologic features. The water bottom in the area is shallow (approximately 100 m depth) and very hard (with reflectivity coefficients as high as 0.4). As illustrated by the observed data shown in Figure 7, these conditions generate a complex mixture of energetic guided waves (red arrows), surface waves in the form of Scholte waves (green arrows), and water-layer-related multiples (blue arrows). Above the chalk, shallow injectites and high-velocity cemented pipes add further complications. All of these features give rise to elastic behavior in the observed data.

To maximize the potential of the observed data, application of FWI in

this area used both the hydrophone (pressure) and geophone (particle velocity) recordings available from the multicomponent OBN acquisition. Utilizing both data sets provided additional constraints to the inversion, helping to optimize the results. In Figure 8, we compare acoustic and elastic FWI at 40 Hz. Both the acoustic (Figure 8b) and elastic (Figure 8c) updated V_p models add significant detail to the smooth starting model (Figure 8a), identifying the cemented pipes (white boxes) and shallow injectites (yellow boxes). The corresponding 40 Hz RTM images (Figures 8d–8f) show a dim zone beneath the cemented pipes (blue boxes) when migrating with the starting model, which is partially repaired when using either of the more accurate models obtained from FWI. Both implementations of FWI capture the broad features of the chalk correctly (black boxes), but elastic FWI offers a much better delineated contrast and reduced velocity “halo” as well as an improved signal-to-noise ratio. On the RTM images, elastic FWI improves the flatness, continuity, and resolution of the chalk layer over acoustic FWI (white arrows).

Figures 8g and 8h show the 40 Hz FWI images corresponding to Figures 8b and 8c, respectively, shown at a larger scale to better highlight the differences between them. While both FWI images show improvements over the RTM imaging, the elastic result exhibits a sharper contrast at the chalk than the acoustic (orange arrows) as well as higher resolution at the seafloor (blue arrows) and reduced noise in the deeper subchalk area in the lower third of the section. Comparison with Figure 8f shows that the remaining dimness underneath the cemented pipes seen on the RTM result is almost completely resolved in the FWI images (blue boxes), with the elastic result again being slightly better than the acoustic. Both FWI images benefit from an increased illumination over the primary-only RTM because they utilize the full wavefield, including diving waves and multiples, as well as automatically compensating for transmission loss effects (Cooper and Ratcliffe, 2023), whereas RTM does not. Overall, we see that the acoustic FWI has performed well in this example despite the challenging geology, generating a result that improves the RTM image and gives further uplift in the FWI image.

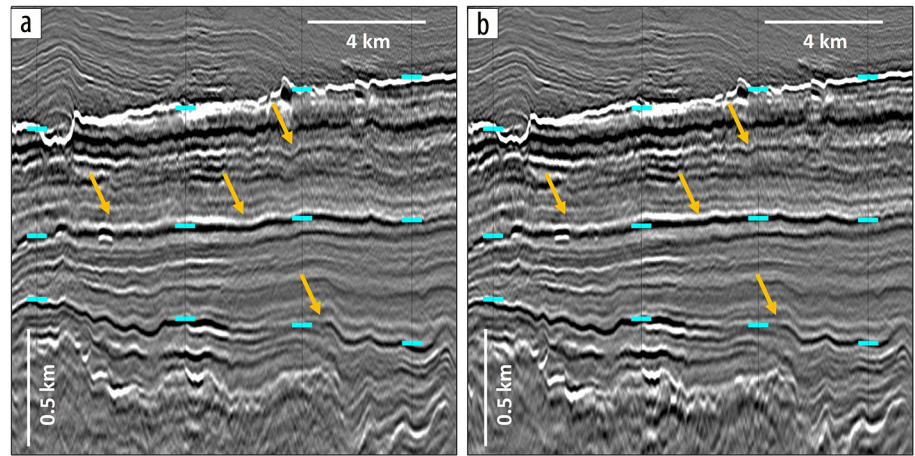


Figure 5. Conventional Kirchhoff prestack depth migration imaging comparison for Golden Eagle using: (a) legacy velocity model and (b) 25 Hz elastic FWI model. Modified from Dobo et al. (2024b).

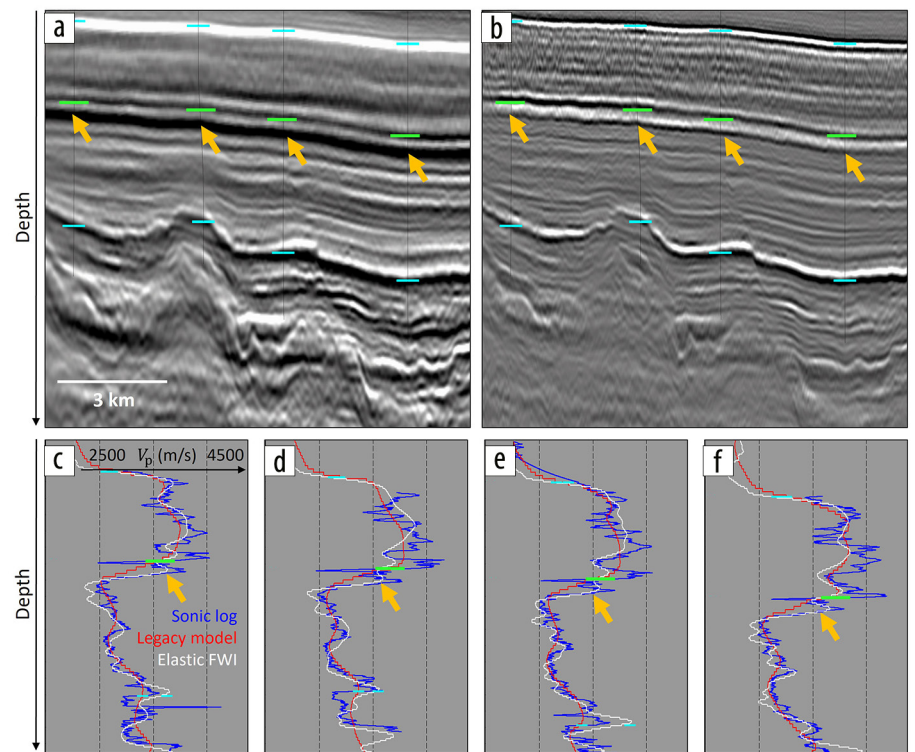


Figure 6. Elastic FWI imaging in the Buzzard area: (a) 30 Hz elastic FWI image, (b) 30 Hz RTM using 30 Hz elastic FWI model, (c)–(f) well logs (blue) compared to elastic FWI model (white) and legacy model (red) for the four well locations highlighted by the markers in (a) and (b). Top and bottom cyan markers highlight the top chalk and Base Cretaceous Unconformity horizons, respectively. Green markers and orange arrows indicate the Plenus Marl and Rødby formations, respectively. Modified from Dobo et al. (2024a).

However, the equivalent results from elastic FWI are slightly better everywhere.

Following the benefits observed with elastic FWI in this area, a targeted follow-up study was conducted recently that focused primarily on the imaging of the Frigg formation above the chalk at a depth of approximately 2 km. Previous attempts to image this formation with acoustic FWI have failed to describe the velocity contrast observed on well logs at this key target horizon. In Figure 9, we compare the results of a 64 Hz elastic FWI with a corresponding RTM in the area where cemented pipes overlie

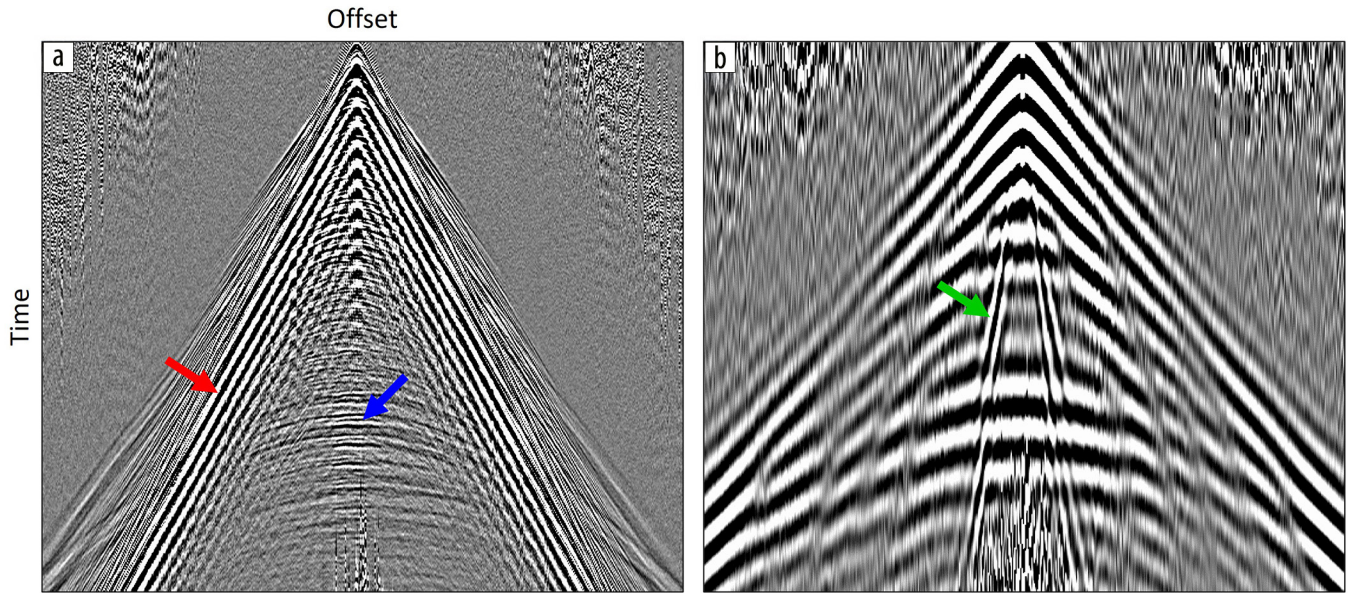


Figure 7. Observed receiver gathers at (a) 40 Hz and (b) 4 Hz, highlighting some of the challenges associated with a highly elastic seabed: guided waves (red arrow), water-layer-related multiples (blue arrow), and Scholte waves (green arrow).

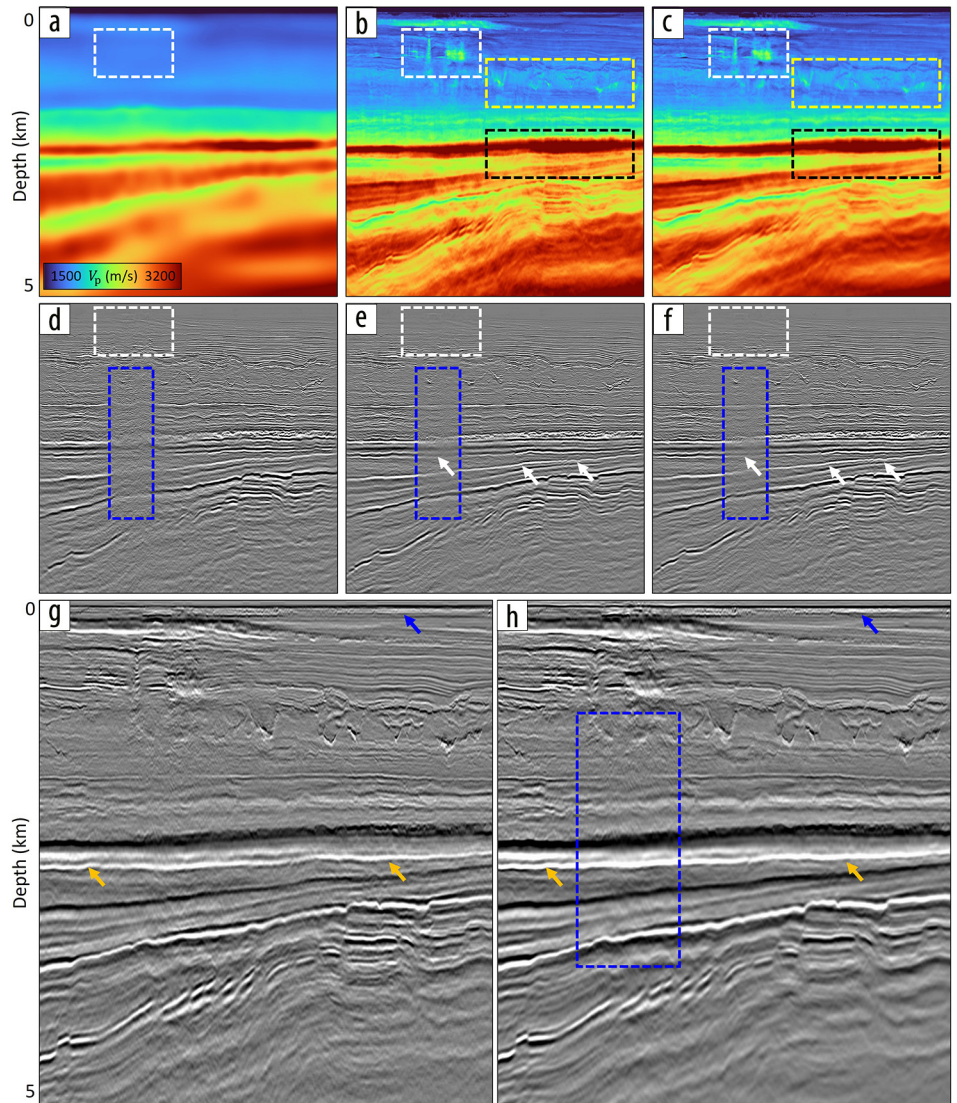


Figure 8. High-resolution acoustic versus elastic FWI in the Norwegian North Sea: (a) starting V_p model; V_p model after (b) 40 Hz acoustic FWI and (c) 40 Hz elastic FWI; (d)–(f) 40 Hz RTM images corresponding respectively to the velocity models in (a)–(c); (g) and (h) 40 Hz FWI images corresponding to the velocity models in (b) and (c), respectively. Modified from Chen et al. (2024).

the top Frigg horizon. The elastic V_p model in Figure 9a shows a well-defined contrast at the Frigg horizon (white box), confirmed by the corresponding FWI image (Figure 9b). The high-resolution FWI image reveals fine layering and significant structural details throughout the shallow section, most notably at the cemented pipes (red box). In contrast, these are either absent or poorly resolved in the corresponding RTM image (Figure 9c). Note that the geologic cementation process is not expected to alter the existing layering structure where the pipes have formed, so it is good to see evidence of event continuity through the pipes in the inverted velocity model. Imaging of the Frigg boundary with elastic FWI is also better than with RTM. This is particularly apparent in the zone directly beneath the cemented pipes, where the blue arrows highlight significant improvements in structural continuity that should help derisk any future exploration and development work.

Discussion

The results presented in this article show a clear trend: the shallower the chalk package becomes, the bigger the impact of the elastic effects in the observed data. Furthermore, for the shallowest chalk examples, we find that acoustic FWI can often fail. Thus, elastic propagation is the essential part of the FWI in these areas. This contrasts with our experience with deeper chalk, where acoustic and elastic FWI can both show uplift over conventional model building approaches, although elastic FWI still provides the superior result. This is true both in the Norwegian North Sea example shown here and in the Central North Sea where salt diapirs cut through deeper chalk (Masmoudi et al., 2022, 2023).

Should we have expected this trend? If so, why? By itself, a chalk layer that is close to the water bottom might not be expected to cause acoustic FWI to fail. This is especially true if advanced cost functions (Zhang et al., 2018) and workflows are used in combination with appropriate data conditioning to mitigate elastic effects in the observed data. Our explanation is that the shallow-water nature of the area exaggerates the differences between acoustic and elastic modeling. For example, consider the first-arrival train of events containing the transmitted energy (diving waves, refractions), the water-bottom reflection, associated guided waves, and likely some other reflections, all of which potentially

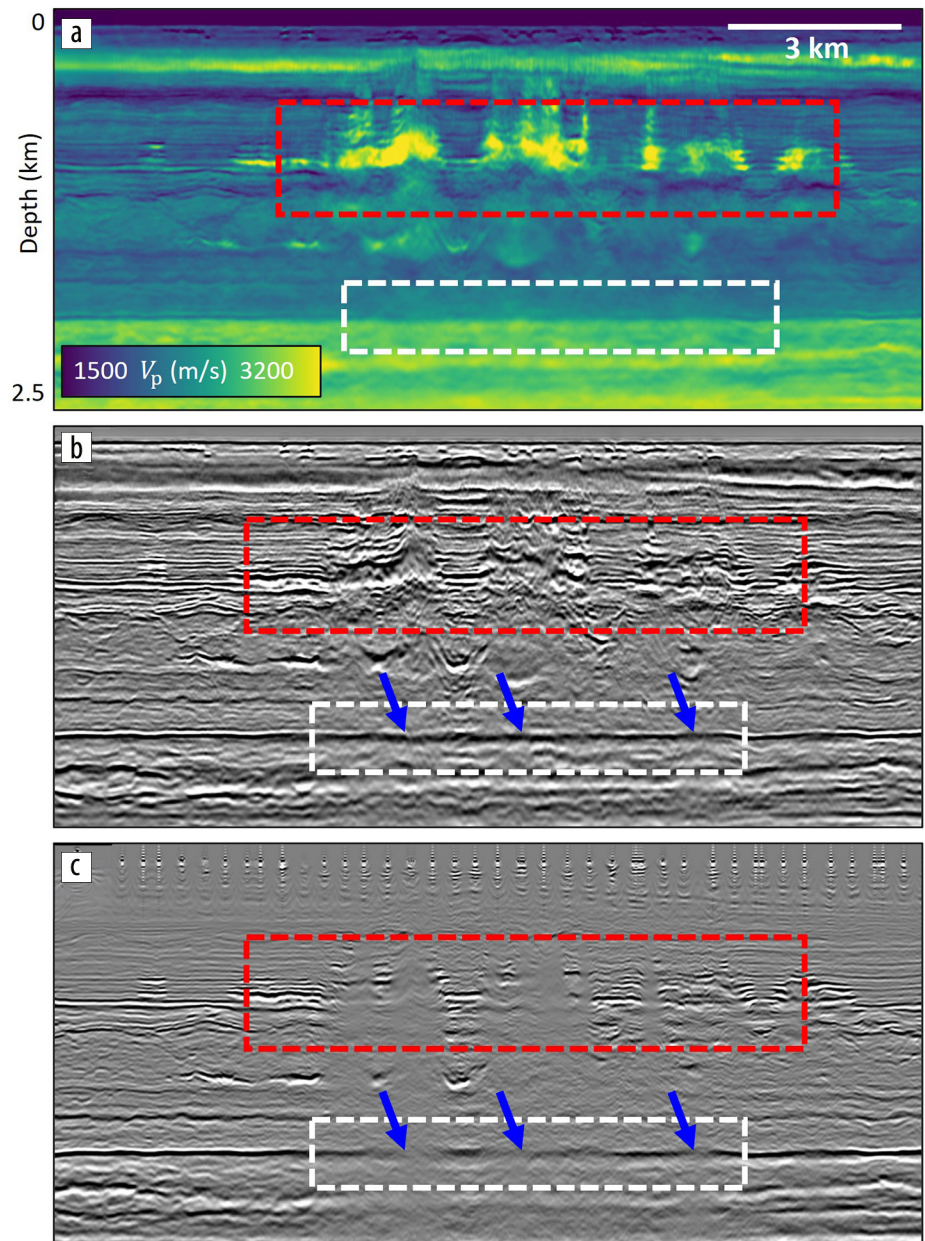


Figure 9. High-resolution elastic FWI around the Frigg formation: (a) V_p model after 64 Hz elastic FWI; (b) corresponding 64 Hz elastic FWI image; (c) corresponding 64 Hz RTM.

contain acoustic/elastic differences. In shallow water, these arrivals concertina and overlap on the modeled gather, so accurately representing the relative amplitude of each arrival becomes critical for correctly describing the interference pattern in the observed data. This is why elastic modeling gives a better agreement with observed data than acoustic, as illustrated by the Breagh example in Figures 1a–1c. We see another example of this phenomena in the Buzzard and Golden Eagle results. When comparing acoustic and elastic FWI in Figure 4, we can see that irregularities in the deeper acoustic FWI velocities are generally worse for Golden Eagle (Figure 4e) than Buzzard (Figure 4a) and that the worst regions correlate to the most rugose parts of the chalk. We attribute this to the more complex interaction of the wavefield with the chalk in these rugose regions, with the elastic modeling naturally

forming a more accurate interference pattern than the acoustic. Finally, we offer a general observation on the elastic FWI results (more clearly seen in the FWI images): that they are slightly cleaner than their acoustic counterparts with improved signal-to-noise. We suggest that this is due to mode conversions being better handled by elastic FWI, whereas they will appear as noise in acoustic FWI, degrading the result.

One key aspect of elastic FWI is the choice of the S-wave velocity (V_S) model and whether this is updated during the P-wave inversion. Here, we use a combination of simple empirical relationships between V_P and V_S (that are appropriate for the local region) and/or estimates from regional well data, with some empirical adjustments for the local geology, for example, chalk or salt bodies. While schemes for S-wave velocity updates using elastic FWI exist (see, for example, Cho et al., 2022; Masmoudi et al., 2024), here we adopt the general strategy of passively maintaining the V_S/V_P ratio, either throughout the inversion or at various QC stages of the model build. Another important factor is the choice of density parameter. Typically, this is based on following a simple Gardner-like power law relation connecting density and P-wave velocity, again with scope to tailor specific regions as needed, such as the water bottom or the chalk interface.

The computational overhead of elastic FWI relative to acoustic means that it is yet to be adopted routinely. However, advances in computational hardware coupled with the development of ever more sophisticated software technologies (such as parallelizing workloads across multiple virtual or physical devices) mean that elastic FWI has progressed rapidly to the point where it can be used directly to inform decisions on active or future field development, even in regions where acoustic FWI offers good value.

Conclusions

We have illustrated the uplift elastic FWI can bring to imaging the complex subsurface in the North Sea region. Key drivers of the need for elastic FWI are the depth of the chalk package, with a greater influence when it is nearer the surface, in tandem with the generally shallow-water nature of this area. Despite being a mature hydrocarbon province, the region is still very active with considerable ongoing exploration and development opportunities. Therefore, elastic FWI offers a way to reduce risk through improved reliability of the structural image and enhanced interpretation coming from the inverted P-wave velocity model. Future improvements could include leveraging S-wave velocity model updates to give additional information for direct reservoir characterization and utilizing multicomponent OBN data to provide additional constraints for the decoupling of different elastic parameters. ■■■

Acknowledgments

We thank INEOS Group Ltd. as licensor of the data and sponsor of the reprocessing, TGS as data owner, and INEOS Group Ltd., ONE-Dyas, and AMK Seismic for permission to show the very shallow chalk example. We thank the coventurers in the Buzzard and Golden Eagle Area developments for permission to show the shallow chalk example: CNOOC Petroleum Europe Limited, Harbour Energy, Equinor, ONE-Dyas, NEO

Energy, and EnQuest PLC. We thank Aker BP and their license partners on PL442 (ORLEN) and PL873 (Equinor and ORLEN) for permission to show the deeper chalk example. Finally, we thank Viridien for permission to publish this work.

Data and materials availability

Data associated with this research are confidential and cannot be released.

Corresponding author: james.cooper@viridiengroup.com

References

- Agudo, O. C., N. V. da Silva, M. Warner, and J. Morgan, 2018, Acoustic full-waveform inversion in an elastic world: *Geophysics*, **83**, no. 3, R257–R271, <https://doi.org/10.1190/geo2017-0063.1>.
- Chen, X., N. Masmoudi, A. Ratcliffe, M. Mallows, and J. Tickle, 2024, Elastic time-lag full-waveform inversion using OBN data in shallow water environments: 85th Conference and Exhibition, EAGE, Extended Abstracts, <https://doi.org/10.3997/2214-4609.202410510>.
- Cho, Y., C. Pérez Solano, J. Kimbro, Y. Yang, R.-E. Plessix, and K. Matson, 2022, Influence of shear velocity on elastic full-waveform inversion: Gulf of Mexico case study using multicomponent ocean-bottom node data: *Geophysics*, **87**, no. 5, R391–R400, <https://doi.org/10.1190/geo2022-0014.1>.
- Cooper, J., and A. Ratcliffe, 2023, The role of FWI imaging in compensating for transmission loss: 84th Conference and Exhibition, EAGE, Extended Abstracts, <https://doi.org/10.3997/2214-4609.2023101288>.
- Dobo, Z., N. Dowd, D. Blake, C. Botondi, N. Masmoudi, A. Ratcliffe, P. McDonnell, B. Tomsett, and T. Sykes, 2024a, Characterizing North Sea chalk with high-resolution elastic full-waveform inversion: 85th Conference and Exhibition, EAGE, Extended Abstracts, <https://doi.org/10.3997/2214-4609.202410453>.
- Dobo, Z., N. Dowd, D. Blake, C. Botondi, A. Ratcliffe, and T. Matic, 2024b, Resolving North Sea chalk complexities with high-resolution elastic full-waveform inversion: Presented at PETEX.
- Dinh, H., T. Latter, M. Townsend, N. Grinde, S. Høgden, N. Robb, M. Aksland, and A. Bertrand, 2024, High-frequency FWI imaging: Repurposing seismic data for imaging shallow hazards: *First Break*, **42**, no. 8, 55–63, <https://doi.org/10.3997/1365-2397.fb2024064>.
- Henin, G., L. Janot, H. Jiang, S. Masclat, N. Salaun, J. E. Lie, V. Danielsen, and P. E. Dhelie, 2023, The road to 200Hz FWI using hybrid streamer and node acquisition over Nordkapp: 84th Conference and Exhibition, EAGE, Extended Abstracts, <https://doi.org/10.3997/2214-4609.202310805>.
- Hobro, J. W. D., C. H. Chapman, and J. O. A. Robertsson, 2014, A method for correcting acoustic finite-difference amplitudes for elastic effects: *Geophysics*, **79**, no. 4, T243–T255, <https://doi.org/10.1190/geo2013-0335.1>.
- Johal, J., M. Oleszuk, N. Masmoudi, A. Ratcliffe, P. Smith, and M. Burbidge, 2024, The benefits of elastic FWI in resolving sub-chalk imaging in the southern North Sea: 85th Conference and Exhibition, EAGE, Extended Abstracts, <https://doi.org/10.3997/2214-4609.202410520>.
- Kalinicheva, T., M. Warner, and F. Mancini, 2020, Full-bandwidth FWI: 82nd Conference and Exhibition, EAGE, Extended Abstracts, <https://doi.org/10.3997/2214-4609.202010246>.
- Lailly, P., 1983, The seismic inverse problem as a sequence of before stack migrations: Proceedings of the International Conference on Inverse Scattering, Theory, and Applications: SIAM.
- Masmoudi, N., W. Stone, A. Ratcliffe, R. Refaat, and O. Leblanc, 2022, Elastic full-waveform inversion for improved salt model building in the central North Sea: 83rd Conference and Exhibition, EAGE, Extended Abstracts, <https://doi.org/10.3997/2214-4609.202211042>.

- Masmoudi, N., W. Stone, and A. Ratcliffe, 2023, Visco-elastic full-waveform inversion and imaging using ocean-bottom node data: 84th Conference and Exhibition, EAGE, Extended Abstracts, <https://doi.org/10.3997/2214-4609.202310497>.
- Masmoudi, N., A. Ratcliffe, O. Bukola, J. Tickle, and X. Chen, 2024, Elastic FWI of multi-component ocean-bottom seismic to update shear-wave velocity models: 85th Conference and Exhibition, EAGE, Extended Abstracts, <https://doi.org/10.3997/2214-4609.202410528>.
- Pérez Solano, C., and R.-E. Plessix, 2023, Can elastic waveform inversion benefit from inverting multicomponent data?: *The Leading Edge*, **42**, no. 3, 184–189, <https://doi.org/10.1190/tle42030184.1>.
- Plessix, R.-E., 2009, Three-dimensional frequency-domain full-waveform inversion with an iterative solver: *Geophysics*, **74**, no. 6, WCC149–WCC157, <https://doi.org/10.1190/1.3211198>.
- Plessix, R.-E., and T. Krupovnickas, 2021, Low-frequency, long-offset elastic waveform inversion in the context of velocity model building: *The Leading Edge*, **40**, no. 5, 342–347, <https://doi.org/10.1190/tle40050342.1>.
- Refaat, R., K. Ubik, J. Sinden, and J. Holden, 2021, Bringing new insights to central North Sea with OBN and FWI imaging: 82nd Conference and Exhibition, EAGE, Extended Abstracts, <https://doi.org/10.3997/2214-4609.202112912>.
- Richardson, J., K. Fu, S. Lu, B. Bai, X. Cheng, and D. Vigh, 2023, Elastic full-waveform inversion on Caesar-Tonga — Case study: *The Leading Edge*, **42**, no. 6, 414–420, <https://doi.org/10.1190/tle42060414.1>.
- Sirgue, L., O. I. Barkved, J. P. van Gestel, O. J. Askim, and J. H. Kommendal, 2009, 3D waveform inversion in Valhall wide-azimuth OBC: 71st Conference and Exhibition, EAGE, Extended Abstracts, <https://doi.org/10.3997/2214-4609.201400395>.
- Sun, B., and T. Alkhalifah, 2021, Pseudoelastic pure P-mode wave equation: *Geophysics*, **86**, no. 6, T469–T485, <https://doi.org/10.1190/geo2021-0084.1>.
- Tarantola, A., 1984, Inversion of seismic reflection data in the acoustic approximation: *Geophysics*, **49**, no. 8, 1259–1266, <https://doi.org/10.1190/1.1441754>.
- Wang, H., O. Burtz, P. Routh, D. Wang, J. Violet, R. Lu, and P. Lazaratos, 2021, Anisotropic 3D elastic full-wavefield inversion to directly estimate elastic properties and its role in interpretation: *The Leading Edge*, **40**, no. 4, 277–286, <https://doi.org/10.1190/tle40040277.1>.
- Wei, Z., J. Mei, Z. Wu, Z. Zhang, R. Huang, and P. Wang, 2023, Pushing seismic resolution to the limit with FWI imaging: *The Leading Edge*, **42**, no. 1, 24–32, <https://doi.org/10.1190/tle42010024.1>.
- Wu, Z., Z. Wei, Z. Zhang, J. Mei, R. Huang, and P. Wang, 2022, Elastic FWI for large impedance contrast: Second International Meeting for Applied Geoscience & Energy, SEG/AAPG, Expanded Abstracts, 3686–3690, <https://doi.org/10.1190/image2022-w17-02.1>.
- Zhang, Z., J. Mei, F. Lin, R. Huang, and P. Wang, 2018, Correcting for salt misinterpretation with full waveform inversion: 88th Annual International Meeting, SEG, Expanded Abstracts, 1143–1147, <https://doi.org/10.1190/segam2018-2997711.1>.
- Zhang, Z., Z. Wu, Z. Wei, J. Mei, R. Huang, and P. Wang, 2020, FWI imaging: Full-wavefield imaging through full-waveform inversion: 90th Annual International Meeting, SEG, Expanded Abstracts, 656–660, <https://doi.org/10.1190/segam2020-3427858.1>.
- Zhang, Z., Z. Wu, Z. Wei, J. Mei, R. Huang, and P. Wang, 2023, Enhancing salt model resolution and subsalt imaging with elastic FWI: *The Leading Edge*, **42**, no. 3, 207–215, <https://doi.org/10.1190/tle42030207.1>.